2020-1

Unsteady Aerodynamic Analysis of Wind Harvesting Aircraft

Judd Mehr
Brigham Young University, juddmehr@gmail.com

Eduardo Alvarez
Brigham Young University, ealvarez@byu.edu

Andrew Ning
Brigham Young University, aning@byu.edu

Unsteady Aerodynamic Analysis of Wind Harvesting Aircraft

Judd Mehr*, Eduardo J. Alvarez*, and Andrew Ning†
Brigham Young University, Provo, Utah, 84602

Airborne Wind Energy (AWE) technology aspires to provide increased options for wind energy harvesting. This includes increased feasibility for temporary and remote installations, as well as the ability to operate at wind speeds both lower and higher than traditional turbines. Additionally, the hope is to be able to produce these extensions of wind energy technology at a lower cost than conventional technologies. As AWE technology is still in its infancy, however, there is very little published information concerning the aerodynamic details of the technology. We have created a set of aerodynamic analysis tools which we apply to wind harvesting aircraft, or windcraft for short, in order to explore some of the basic aerodynamic performance properties of a rigid-wing, on-board generation AWE platform, similar to the Makani M600 prototype. In this work, we perform an introductory exploration of the aerodynamics of a windcraft first in steady, level flight, then following a circular path in cross-wind flight. Positive interactions between the upper and lower rotor wakes increase the overall wing lift in the steady, level case by an average of 5.3 percent relative to the wing without rotors present. In addition to the same positive interactions between upper and lower rotors, the cross-wind orientation of the circular path leads to the rotor wakes being pushed "up" relative to the wing, leading to an additional increase in force. Specifically, the normal force of the wing with rotors in the circular path is increased by an average of 17.3 percent relative to the wing in the same path without rotors.

I. Introduction

The typical three-blade turbine design, like the one pictured in figure 1, is the result of many years of research, engineering, and optimization. This design, however, requires a large amount of extraneous structure that does not directly contribute to the energy-gathering potential of the turbine, and can be prohibitive when it comes to site selection and construction of larger turbines. In the 1970s, interest formed in developing technology that did not require as much extraneous mass. Researchers focused on how it might be possible to eliminate nearly everything but the blade tips (where the majority of energy is extracted)—the overall goal being a reduction of both cost and installation difficulties. This interest culminated in the well known 1980 paper by Loyd [1], detailing initial concepts for crosswind kite power technology, now commonly called Airborne Wind Energy (AWE) technology. Shortly after, AWE development was more or less shelved for roughly twenty years until it came back into the limelight in the early 2000s. In addition to potential cost savings, recent interest in AWE technology also notes the potential benefits in installation flexibility. Such flexibility could allow for temporary installations, installations in remote locations both on and off shore, and in locations where wind speeds are too high and/or too low for traditional turbines to be effective.

Various designs have been considered since the conception of AWE technology [2], including both lift and drag based power generation [3, 4], soft [5, 6] and rigid [7] "kite" structures, lighter- [8, 9] and heavier-than-air designs, single and multi-kite [10, 11] implementations, as well as other unconventional designs [12–14]. De Lellis, Reginatto, Saraiva, and Trofino found that the theoretical efficiency limit of AWE systems matches that of conventional wind turbines [3]. Kheiri, Nasrabad, and Bourgault compared lift- and drag-based systems and determined that drag-based systems have the potential to produce greater amounts of power than lift-based systems [4]. Looking specifically at soft kite technology, Folkersma, Schmehl, and Viré found that delaying separation or tripping turbulence over the kite at different phases of flight could improve the

Fig. 1 Photograph of a modern wind turbine, courtesy of the United States Air Force.

---

overall system performance [5]. Thedens, Oliveira, and Schmehl looked at the deformation of soft kites and found that optimizing using fluid structure interaction models was important for designing kites for actual operation [6]. Fagiano and Schnez explored vertical takeoff of rigid-wing systems, finding that takeoff vertically is a viable approach [7]. Saeed and Kim look at buoyant shell systems and reported the aerodynamic performance on a simulated shell body [8]. Cobb, Deodhar, and Vermillion did experimental work on buoyant shell turbines and found that operation in controlled cross-wind flight patterns outperformed stationary operation for buoyant shell systems [9]. Zanon et al. studied configurations with multiple wings on the same primary tether and found it to be advantageous for smaller sized setups, but less advantageous for larger systems [10, 11]. The applicability of AWE technology has also been explored through studies relating to global wind patterns in which it was found that AWE technology is physically viable with the wind resources available [15–17]. The majority of published studies on AWE technology are concerned with the complex control systems required to operate AWE systems, several papers being published for each of the various designs mentioned. However, this paper deals with aerodynamics rather than controls.

Specifically, our focus in this research is primarily the aerodynamic analysis of rigid-wing "kites" that we term as wind harvesting aircraft, or more simply, *windcraft*. Our terminology is inspired by obvious similarities to standard fixed-wing aircraft (see figure 2) combined with differences inherent to wind energy harvesting applications. More specifically, in this work we focus on a drag-based (on-board generation) windcraft system.

In the literature, as far as we are aware at the time of publication, only one published study involves a complete, drag-based, multi-rotor design [18], which focuses on the aerostructural characteristics of a bridled windcraft. Another study involving drag-based AWE systems extends the actuator disc theory to drag-based AWE designs, but does not explore the aerodynamic details of an actual windcraft [19]. More work on detailed aerodynamics has been accomplished with lift-based systems such as a study by Fasel, Keidel, Molinari, and Ermanni that uses panel methods for the aerodynamics of an aerostructural optimization of morphing wings applied to AWE [20]. They also applied their tools later, with Tiso as an additional co-author, to create a framework for coupled aerostructural and dynamic optimization of lift-based systems [21]. Other analyses have been done on buoyant-shell turbines. For example, Saleem and Kim apply Reynolds-averaged Navier-Stokes solver to buoyant shell turbines to compare the power coefficients of three different designs [22]. Saeed and Kim explore the realignment behavior of a similar design at different wind speeds using ANSYS software for a fully coupled fluid-structure analysis [23]. In this study, we seek to analyze the basic aerodynamics of windcraft, specifically looking at how the lift of the wing is affected by rotors extracting energy from the flow over the wing. To do so, we employ the combination of a vortex particle method (VPM), vortex lattice method, and a blade-element momentum method in exploring the drag-based windcraft design space.
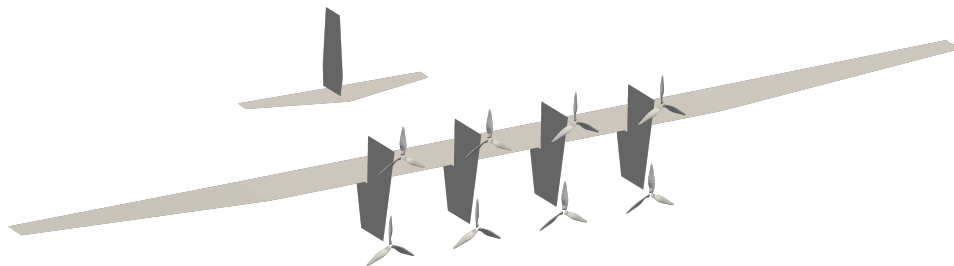
II. Models

Fig. 2   A visual representation of the approximation of the Makani M600 Windcraft geometry used in this work. Geometry details can be found in appendix A.

A. Windcraft Geometry

Despite scarcity of detailed aerodynamic analyses of drag-based windcraft in the literature, one of the most publicized contributor to windcraft technologies is the Makani company, whose latest prototypes and proposed designs are drag-based. For this study, we roughly approximated the geometry of the Makani M600 prototype from publicly available images. Figure 2 shows our representation of the geometry, and detailed information for our model geometry can be found in appendix A. Note that the full volumetric geometry is unnecessary for our model since we are using

a vortex lattice method for the lifting surfaces. Thus, we are satisfied with a surface representation of the windcraft geometry. Furthermore, we neglected the tail boom and generator nacelles (located just behind the rotors) in this study.
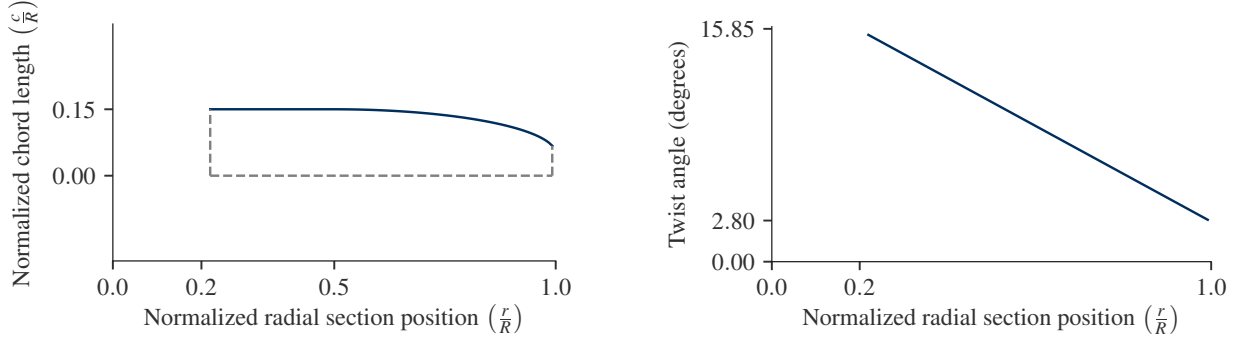
(a) The rotor blade chord distribution, based on estimates from publicly available images. Note that the straight leading edge is along the zero line.

(b) The optimal rotor blade twist distribution when maximizing coefficient of power in a turbine usage case.

Fig. 3 To define the rotor blade geometry, we first made estimates of the chord distribution based on public images of the rotors. We then performed an optimization to find the twist distribution providing the maximum power coefficient for power generation.

For the rotor geometry, we again referenced publicly available images of the M600 to approximate the diameter (two meters) and chord distribution. We assumed a straight leading edge for the blades, and estimated the chord distribution, c, to be

$$c\left(r/R\right) = \begin{cases} 0.15 & 0.2 \leq r/R < 0.5 \\ 0.05 + \frac{1}{10}\left[1 - (2\left(r/R\right) - 1)^2\right]^{1/2} & r/R \geq 0.5 \end{cases} \tag{1}$$

for normalized radial stations, r/R (where R is the radius at the rotor blade tip). Equation (1) comes from an elliptical profile for which we matched the normalized root chord value (an estimated 0.15), the length over which we desired the curve to be defined, and a normalized tip chord of 0.05. For radial positions less than or equal to 50% of the total rotor radius, we defined the chord to be equal to the root chord value. Note that the rotor hub extends to $r/R = 0.2$, so the chord is only defined over the range [0.2, 1.0]. Also note that we defined the leading edge location to be a constant across the blade as this seemed an appropriate approximation of the Makani rotor blades. As no information is available concerning the airfoil cross-sections of the Makani rotors, we chose a NACA 0012 airfoil due to its symmetric profile and readily available data. A symmetric airfoil easily allows for both energy capture and propulsion capabilities without additional consideration. In this study, however, we focused on energy capture when defining the rotor geometry.

In order to define a blade twist distribution, we first assumed a linear distribution and then performed the simple optimization described in equation (2).

$$\begin{aligned} \text{maximize} &: \ C_P \\ \text{w.r.t.} &: \ \theta_0, \ \frac{d\theta}{dr}, \lambda \end{aligned} \tag{2}$$

where C_P is the power coefficient of the rotor operating as a turbine, θ_0 is the root twist value, $d\theta/dr$ is the linear change in twist along the blade, and λ is the tip speed ratio. The optimized linear distribution for maximal power generation came out to be

$$\theta\left(r/R\right) = 0.332 - 0.284\left(r/R\right) \tag{3}$$

where θ is the twist angle in radians and r is again the radial location along the blade. Note that we did not include any precone angle for this rotor design. We have included plots of the chord and twist distributions in figure 3. We also included the power generation coefficient and drag coefficient plots for the rotor in figure 4. It should be noted that in wind turbine nomenclature, the rotor drag coefficient is usually labeled as a thrust coefficient in the turbine reference
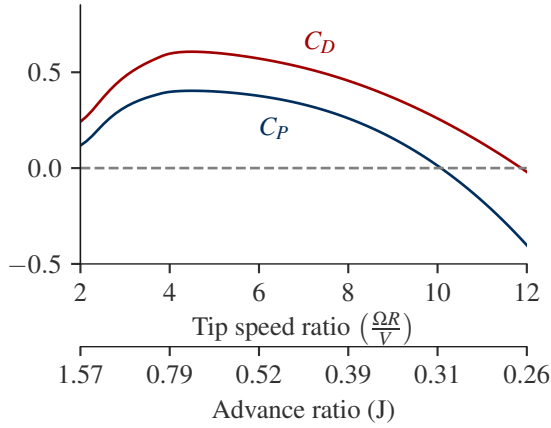
3

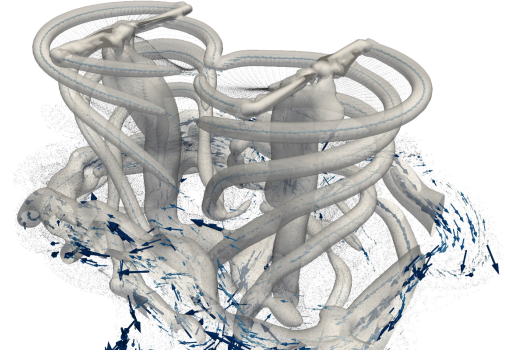**Fig. 4 Power (generated) and drag coefficients vs. tip speed ratio and advance ratio for the rotor.**

Fig. 5 An example of propeller simulation in a multi-rotor configuration. The points show the position vortex particles and the arrows show the vortex strength of each particle. Additionally, the iso-surfaces are superimposed.

frame. Here we have chosen to label it as drag to identify the thrust producing region (where the rotor transitions from generating to expending power).

Our model employs three blades, rather than the five pictured on the Makani prototype, for the purpose of increased wake stability in order to be able to obtain more useful data in simulation. It should be noted that we optimized our rotor solely for maximizing energy extraction. In practice, rotors must be able to produce sufficient thrust for windcraft takeoff, but for the purposes of this study, we focus solely on power generation.

B. Simulation Models

The following models are part of the simulation suite, *FLOWUnsteady**, developed by members of the Brigham Young University Flight Optimization and Wind Laboratory.

1. Viscous Vortex Particle Method (VPM)

The viscous vortex particle method can be described as a mesh-free, computational fluid dynamics method for the solution of the vorticity form of the Navier-Stokes equations. This form of the Navier-Stokes equations comes from taking the curl of the typical momentum formulation. By mesh-free, we mean that this method is set in a Lagrangian, rather than an Eulerian, numerical scheme. Detailed explanations of the theory and implementation of this method are available in [24, 25].

2. Propeller Model

The propeller model we use is also described in detail in previous work [25, 26]. The propeller model initializes by discretizing the geometry into blade elements, calculating airfoil characteristics on those elements through XFOIL, and applying a compressibility correction factor and post-stall extrapolations. It then sheds vortex particles from the trailing edge of each blade as rotors rotate and translate in space. Thus, the vorticity form of the Navier-Stokes equation is resolved, capturing all unsteady dynamics in the wake through the VPM, while calculating unsteady aerodynamic forces through the blade elements. As an example, figure 5 shows the simulation of two propelling rotors in hover using this model [25, 26].

#### 3. Unsteady Lifting-surface Model

In order to model the lifting surfaces (with the exception of the propellers just described) we employed a vortex lattice method. We implemented this in the typical manner, prescribing a lattice of vortex elements placed at the quarter-chord with control points at the three-quarter-chord. Our model allows for rotor-on-wing, wing-on-wing, and

---

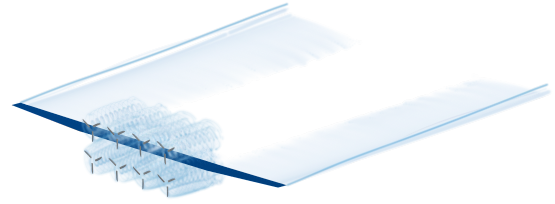*https://github.com/byuflowlab/FLOWUnsteady

4

wing-on-rotor interactions by allowing for an unsteady input velocity as well as reincorporating the induced vorticity back into the particle field. See [27] for more details on the implementation.

III. Studies

A. Steady, Level Flight
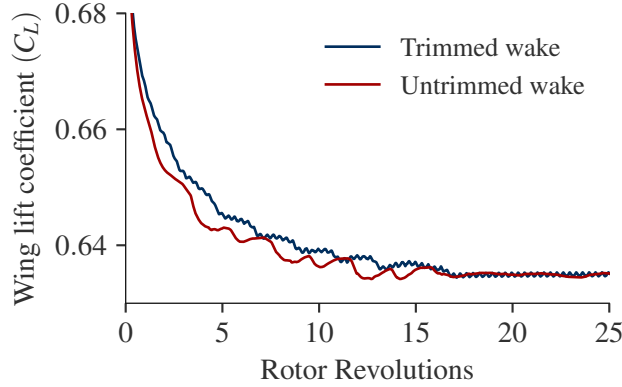
(a) The convergence of the trimmed wake (see (b)) matches well with that of the untrimmed wake.

(b) The trimmed wake has particles removed one chord length from the trailing edge, where we employ disk-shaped cutting planes that are twice the rotor radius and aligned with the rotor axes. In addition, the entire wake is removed one span downstream from the wing trailing edge.

Fig. 6   Despite trimming the inboard portion of the wake, allowing the outboard portion to grow a full span downstream allows for good matching of the untrimmed case.

To get an introductory view of the overall aerodynamic performance of the windcraft, we began by exploring a simple level trajectory to which we compared a circular path, described below. We used a freestream of 50 m/s with an angle of attack of four degrees to match the circle case with its cross-wind flight state. We should note that, for simplicity of this initial study (as well as the circular path study below), we did not include the tail structure and pylons, focusing our study on characterizing rotor-on-wing and wing-on-wing aerodynamic interactions.

We chose to run the rotor at a constant tip speed ratio of 4.0 (equivalent to a an RPM of approximately 1527 and Mach number of approximately 0.074 at the blade tip), as that was close to where our rotor is most efficient in energy extraction (see figure 4) and where we had sufficient numerical stability for this study. In order to simulate the windcraft, we applied the aforementioned simulation tools employing the following parameters. We chose to use seven blade elements per rotor blade, as this gave an acceptable resolution without major computational requirements. For the vortex particle method, we chose to use 72 time steps per rotor revolutions, shedding two particles from each blade element per time step. This moderately fine step size with multiple particle shedding kept the simulation stable, but lower resolution might be possible for faster computation in future studies. Following the suggestions in [26] we used a core overlap factor of 2.125, and a relaxation factor for our vortex lattice method of 0.25. These allowed our wake to remain stable sufficiently long to obtain the desired data. We used 52 horseshoe vortex lattice elements (two per meter for our geometry) on the main wing.

Due to the turbulent breakdown of the wake that takes place more than one chord-length downstream, we found it necessary to trim the rotor wakes one chord-length aft of the wing trailing edge. Trimming the wake was necessary to maintain the numerical stability of the simulation sufficiently long to obtain useful data. We cut the wake using disk profiles with a two meter radius behind each rotor, thus allowing the wing tip wake to develop normally. As mentioned above, we also performed this study with three-bladed rotors rather than the five-bladed rotors that the Makani M600 prototype uses. The purpose for this was to delay the rotor wake turbulent breakdown to be further downstream than our cutoff point. In order to decrease computational costs, we also cut the entire wake one span-length downstream from the wing trailing edge. We found, as shown in figure 6a, that one span gave us a good approximation of an uncut wake.

Figure 6b shows an example of a fully developed, cut wake from our simulations.

We also explored how long our simulations needed to run in order to achieve statistically stationary output data. By observation of figure 8, which shows a time-averaged plot of wing normal force coefficient vs rotor revolutions, we found that our simulations achieved stationarity after roughly 20 rotor revolutions.

B. Circular Path Performance

For the circular path we defined an overall path diameter of 135 meters, a total tether length of 440 meters, and an inclination angle of 0.4 radians (approximately 20 degrees) measured from the orbit axis (see figure 7). We set the freestream velocity to be 3.5 m/s, which is simply an arbitrary starting point. We approximated the vehicle velocity to vary sinusoidally between 30 m/s at the top of the path, and 50 m/s at the bottom. We also assumed that energy generation takes place for the entirety of the path. Although in practice this has yet to be accomplished with an on-board generation windcraft design, this is the goal of the technology, and we can still obtain useful results with this simplification. In this study, we focused on the bottom portion of the circle, ending at the bottom of the path, in order to study the effects of the turbines on the wing performance at the extreme of a realistic flight path (based on publicly available test flight recordings). We used the same simulation settings as we did in the steady, level case, keeping the tip speed ratio constant.
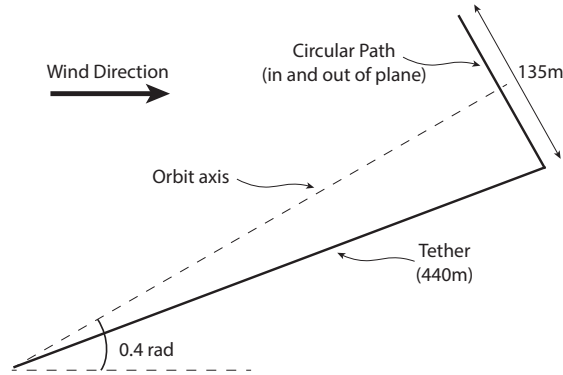

Fig. 7   Circular path geometry for initial windcraft flight analysis.

Note that for the steady, level case, we look at lift force, as lift is an intuitive value for this case. On the other hand, for the circular path, which is neither steady, nor level, lift no long has an intuitive meaning. For this purpose, we look at the normal force rather than the lift. That is, the force normal to the wing surface at the wing root.

IV. Results

Figure 8 shows the average lift over 50 rotor revolutions, and figure 9 shows an example lift distribution, for the steady, level flight case. Note that despite the instantaneous lift distribution having values both above and below the nominal (without rotors) wing lift, the overall trend is that the presence of rotors increases the lift relative to the nominal lift. Interestingly, this phenomena is typical for in-line propeller configurations that are imparting momentum to the flow over the wing. In our case, however, the rotors are decreasing the overall fluid momentum as they extract energy.

Examining figure 10, we see more specifically what causes the overall increase in normal force. Without rotors, the velocity gradient across the wing is linear. When rotors are added as we have done here, however, the upper and lower rotors tend to entrain additional velocity between them, such that as the wakes pass over the wing, the wing sees an increase in velocity. On the other hand, between the rotors laterally, the velocity decreases. Comparing with figure 12, we see that averaged over time, the increased velocity between the top and bottom wakes outweighs the decreased velocity between the side-by-side wakes, thereby giving an overall average increase in normal force.

Averaging the forces over the range from 25 to 50 rotor revolutions, the overall mean difference for the steady, level case is 0.56 kN of lift (a 5.3 percent increase from nominal). Looking at the circle case, we find similar trends along with some differences from the steady, level case.

In the circle path case, the wind pushes the wakes "up" relative to the windcraft reference frame. This causes the wakes from the lower rotors to get pushed into the wing, while the upper rotor wakes are pushed away from the aircraft
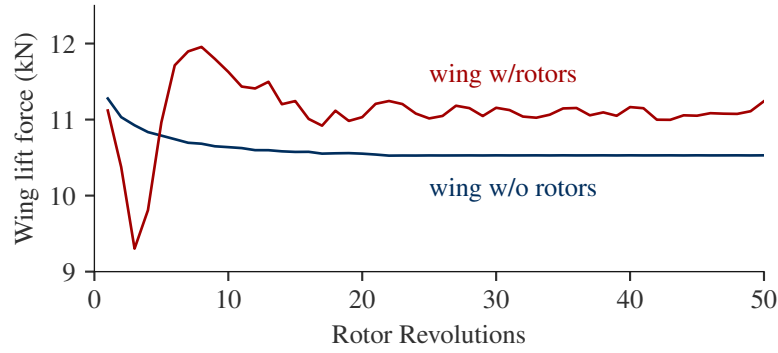
Fig. 8 The time averaged lift convergence shows that a positive interaction increases the total wing lift coefficient when rotors are present. Note that here the lift coefficient is averaged over sets of 72 time steps, or single rotor revolutions.
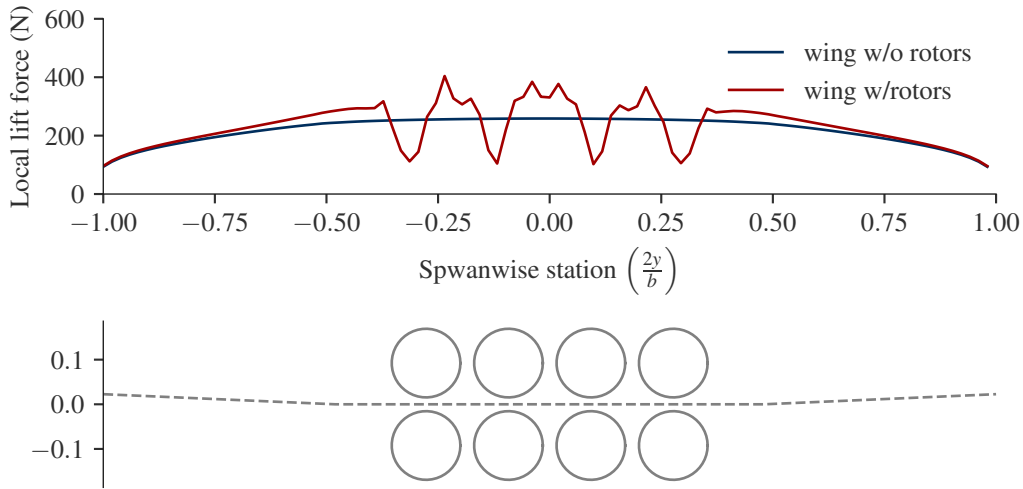

Fig. 9 An example instantaneous lift distribution for the steady, level flight path. Shown in gray below are the rotor positions (solid lines) relative to the wing (dotted lines).
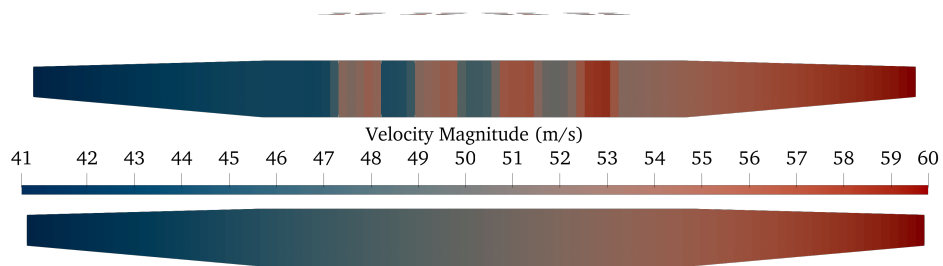

Fig. 10 Comparison of the instantaneous velocity magnitude, in meters per second, over the wing with and without rotors at the bottom of the circular path for a single time step. Without rotors (bottom), the velocity gradient across the wing is linear. With rotors (top), however, the upper and lower rotors entrain additional velocity between their wakes.

(see figure 11). As shown in figures 12 and 13a, the trends are similar to the steady, level flight case, such that the overall normal force of the wing with rotors is greater than that of the wing without rotors in the same trajectory. The average

difference over 25 rotor revolutions is 3.4 kN (17.3 percent greater than nominal). The circular trajectory also skews the velocity of the wing causing the normal force distribution to be non-symmetric. That is, the portion of the wing closer to the center of the circular path is naturally traveling slower than the portion toward the outside of the circular path. This causes a linear velocity gradient across the wing as seen in the lower half of figure 10.

(a) Rotor wakes for steady, level flight tend to go more or less straight back.

(b) Rotor wakes for circle path, tend to be pushed "up" relative to the windcraft wing, while also being left behind in the circular path (see figure 11c).

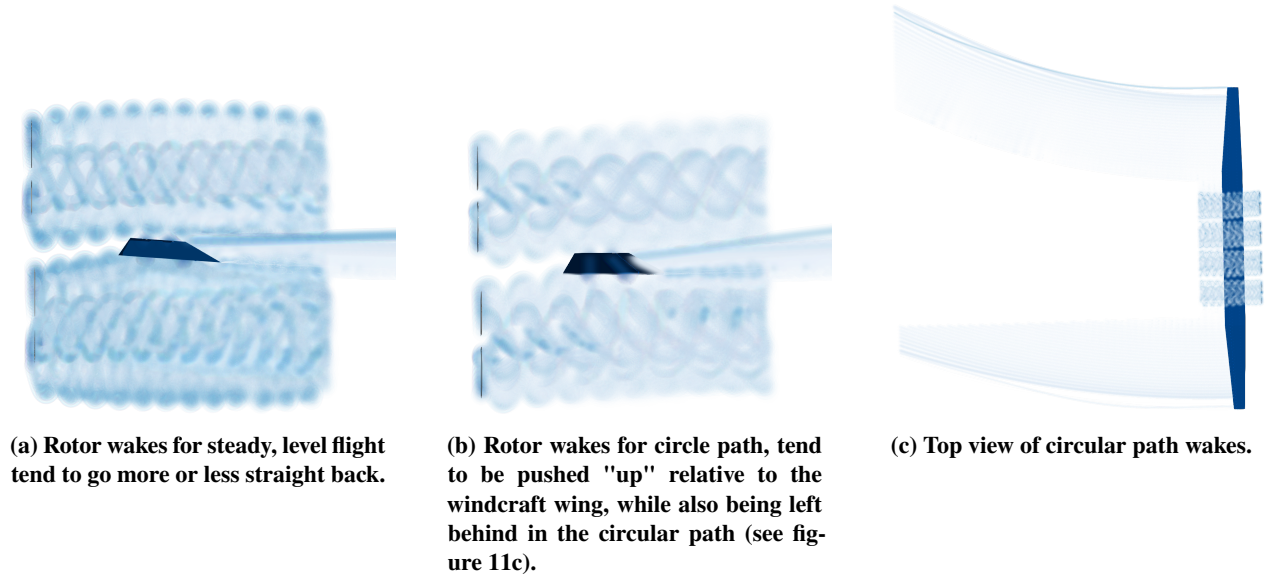(c) Top view of circular path wakes.

Fig. 11   The wake behavior in the circle path differs from that of steady, level flight in that the rotor wakes are pushed normal to the wing surface by the crossing wind, and the rotor wakes are left slightly to the side (see figure 11c) of the rotor axis as the windcraft rotates. Note in these figures that the dark trapezoidal shape is the silhouette of the wing side profile.
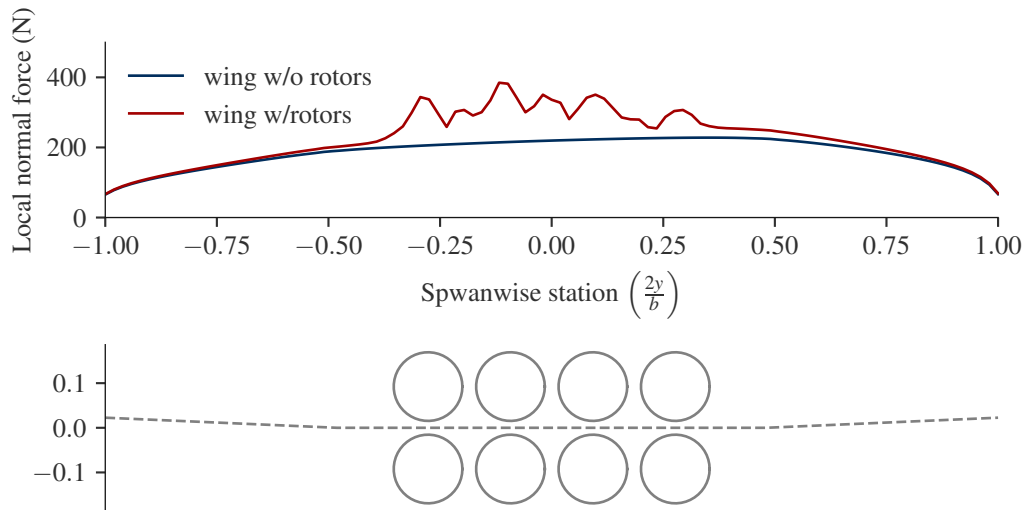

Fig. 12   The normal force distribution for the windcraft in a circle path is skewed toward the outboard side due to the velocity gradient in the circle path. That is, the outboard part of the wing travels faster than the inboard section when traveling in a circle. Shown here is the normal force distribution averaged over 25 rotor revolutions from revolution 25 to 50. Shown in gray below are the rotor positions (solid lines) relative to the wing (dotted lines).
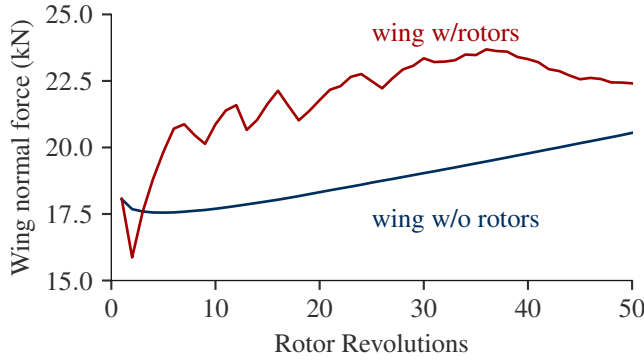
(a) The normal force coefficient on the wing over a simulation lasting 50 rotor revolutions.
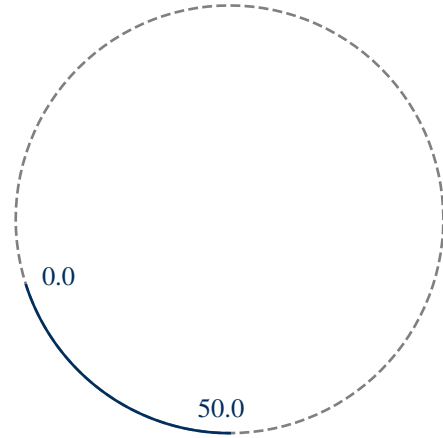
(b) The portion of the circular path traversed during this simulation.

Fig. 13 **The path starts at zero rotor revolutions (with a windcraft speed of just approximately 42 m/s), and ends at the bottom of the path after roughly 50 rotor revolutions (and a windcraft speed of 50 m/s). The overall normal force on the wing increase for the circle path as the velocity increases from lower (at the top of the path) to higher (at the bottom of the path).**

V. Conclusion and Future Work

The rotors in this configuration increase the overall lift of the wing—similar to what can be seen for propellers blowing on a wing in an in-line configuration. Even though the rotors here are extracting energy and decreasing the momentum of the overall velocity field, the rotor wakes are entraining increased velocity between the upper and lower rows, effectively increasing the velocity seen by the wing.

With direction from the results presented, we plan to perform a more detailed exploration of the design space to better understand the validity and impacts of this and other windcraft configurations and operational states. We plan to explore more configurations, including rotors in-line with the wing, various velocities and tip speed ratios, different rotation directions for each rotor, etc. We have also found that rotor design for windcraft technologies appears to be an unstudied, but potentially rich area of research, and we plan to include more robust rotor design in future works. In addition, we anticipate adding some level of controls to the windcraft to allow for greater accuracy in the trajectory. Finally, we anticipate adding a boundary element method (panel method) to model such things as the tail boom and rotor nacelles in future research.

VI. Acknowledgments

9

References

[1] Loyd, M. L., "Crosswind Kite Power," *Journal of Energy*, Vol. 4, No. 3, 1980, pp. 106–111.

[2] Cherubini, A., Papini, A., Vertechy, R., and Fontana, M., "Airborne Wind Energy Systems: A review of the technologies,", 2015. doi:10.1016/j.rser.2015.07.053.

[3] De Lellis, M., Reginatto, R., Saraiva, R., and Trofino, A., "The Betz limit applied to Airborne Wind Energy," *Renewable Energy*, Vol. 127, 2018, pp. 32–40. doi:10.1016/j.renene.2018.04.034.

[4] Kheiri, M., Saberi Nasrabad, V., and Bourgault, F., "A new perspective on the aerodynamic performance and power limit of crosswind kite systems," *Journal of Wind Engineering and Industrial Aerodynamics*, Vol. 190, No. April, 2019, pp. 190–199. doi:10.1016/j.jweia.2019.04.010.

[5] Folkersma, M., Schmehl, R., and Viré, A., "Boundary layer transition modeling on leading edge inflatable kite airfoils," *Wind Energy*, Vol. 22, No. 7, 2019, pp. 908–921. doi:10.1002/we.2329.

[6] Thedens, P., de Oliveira, G., and Schmehl, R., "Ram-air kite airfoil and reinforcements optimization for airborne wind energy applications," *Wind Energy*, Vol. 22, No. 5, 2019, pp. 653–665. doi:10.1002/we.2313.

[7] Fagiano, L., and Schnez, S., "On the take-off of airborne wind energy systems based on rigid wings," *Renewable Energy*, Vol. 107, 2017, pp. 473–488. doi:10.1016/j.renene.2017.02.023.

[8] Saeed, M., and Kim, M. H., "Aerodynamic performance analysis of an airborne wind turbine system with NREL Phase IV rotor," *Energy Conversion and Management*, Vol. 134, 2017, pp. 278–289. doi:10.1016/j.enconman.2016.12.021, URL `http://dx.doi.org/10.1016/j.enconman.2016.12.021`.

[9] Cobb, M., Deodhar, N., and Vermillion, C., "Lab-scale experimental characterization and dynamic scaling assessment for closed-loop crosswind flight of airborne wind energy systems," *Journal of Dynamic Systems, Measurement and Control, Transactions of the ASME*, Vol. 140, No. 7, 2018, pp. 1–12. doi:10.1115/1.4038650.

[10] Zanon, M., Gros, S., Andersson, J., and Diehl, M., "Airborne Wind Energy Based on Dual Airfoils," *IEEE Transactions on Control Systems Technology*, Vol. 21, No. 4, 2013, pp. 1215–1222.

[11] Zanon, M., Gros, S., Meyers, J., and Moritz, D., "Airborne Wind Energy : Airfoil-Airmass Interaction," *The International Federation of Automatic Control*, Capte Town, South Africa, 2014, pp. 5814–5819. doi:10.3182/20140824-6-ZA-1003.00258.

[12] Milutinović, M., Čorić, M., and Deur, J., "Operating cycle optimization for a Magnus effect-based airborne wind energy system," *Energy Conversion and Management*, Vol. 90, 2015, pp. 154–165. doi:10.1016/j.enconman.2014.10.066.

[13] Pavković, D., Cipek, M., Hrgetić, M., and Sedić, A., "Modeling, parameterization and damping optimum-based control system design for an airborne wind energy ground station power plant," *Energy Conversion and Management*, Vol. 164, No. March, 2018, pp. 262–276. doi:10.1016/j.enconman.2018.02.090.

[14] Mackertich, S., "Dynamic Modeling of Autorotation for Simultaneous Lift and Wind Energy Extraction," Ph.D. thesis, University of Central Florida, 2016.

[15] Archer, C. L., Delle Monache, L., and Rife, D. L., "Airborne wind energy: Optimal locations and variability," *Renewable Energy*, Vol. 64, 2014, pp. 180–186. doi:10.1016/j.renene.2013.10.044, URL `http://dx.doi.org/10.1016/j.renene.2013.10.044`.

[16] Bechtle, P., Schelbergen, M., Schmehl, R., Zillmann, U., and Watson, S., "Airborne wind energy resource analysis," *Renewable Energy*, Vol. 141, 2019, pp. 1103–1116. doi:10.1016/j.renene.2019.03.118, URL `https://doi.org/10.1016/j.renene.2019.03.118`.

[17] Sommerfeld, M., Crawford, C., Monahan, A., and Bastigkeit, I., "LiDAR-based characterization of mid-altitude wind conditions for airborne wind energy systems," *Wind Energy*, Vol. 22, No. 8, 2019, pp. 1101–1120. doi:10.1002/we.2343.

[18] Wijnja, J., Schmehl, R., De Breuker, R., Jensen, K., and Lind, D. V., "Aeroelastic analysis of a large airborne wind turbine," *Journal of Guidance, Control, and Dynamics*, Vol. 41, No. 11, 2018, pp. 2374–2385. doi:10.2514/1.G001663.

[19] Kheiri, M., Bourgault, F., Nasrabad, V. S., and Victor, S., "On the aerodynamic performance of crosswind kite power systems," *Journal of Wind Engineering and Industrial Aerodynamics*, Vol. 181, No. April, 2018, pp. 1–13. doi:10.1016/j.jweia.2018.08.006.

[20] Fasel, U., Keidel, D., Molinari, G., and Ermanni, P., "Aerostructural optimization of a morphing wing for airborne wind energy applications," *Smart Materials and Structures*, Vol. 26, 2017. doi:https://doi.org/10.1088/1361-665X/aa7c87.

[21] Fasel, U., Tiso, P., Keidel, D., Molinari, G., and Ermanni, P., "Reduced-Order Dynamic Model of a Morphing Airborne Wind Energy Aircraft," *AIAA Journal*, Vol. 57, No. 8, 2019, pp. 3586–3598. doi:10.2514/1.j058019.

[22] Saleem, A., and Kim, M. H., "Aerodynamic analysis of an airborne wind turbine with three different aerofoil-based buoyant shells using steady RANS simulations," *Energy Conversion and Management*, Vol. 177, No. April, 2018, pp. 233–248. doi:10.1016/j.enconman.2018.09.067, URL https://doi.org/10.1016/j.enconman.2018.09.067.

[23] Saeed, M., and Kim, M. H., "Airborne wind turbine shell behavior prediction under various wind conditions using strongly coupled fluid structure interaction formulation," *Energy Conversion and Management*, Vol. 120, 2016, pp. 217–228. doi: 10.1016/j.enconman.2016.04.077, URL http://dx.doi.org/10.1016/j.enconman.2016.04.077.

[24] Alvarez, E. J., and Ning, A., "Development of a Vortex Particle Code for the Modeling of Wake Interaction in Distributed Propulsion," *2018 Applied Aerodynamics Conference*, American Institute of Aeronautics and Astronautics, 2018, pp. 1–22. doi:10.2514/6.2018-3646, URL https://arc.aiaa.org/doi/10.2514/6.2018-3646.

[25] Alvarez, E., and Ning, A., "Modeling Multirotor Aerodynamic Interactions Through the Vortex Particle Method," *AIAA Aviation Forum*, 2019, p. 3191. doi:10.2514/6.2019-2827, URL https://scholarsarchive.byu.edu/facpubhttps://scholarsarchive.byu.edu/facpub/3191.

[26] Alvarez, E. J., and Ning, A., "High-fidelity Modeling of Multirotor Aerodynamic Interactions for Aircraft Design," *AIAA Journal*, 2020. (accepted).

[27] Alvarez, E. J., "FLOWUnsteady Documentation: Development of an Unsteady Mixed-fidelity Aerodynamics Solver for Maneuvering Multirotor Aircraft," , June 2020. URL https://github.com/byuflowlab/FLOWUnsteady.
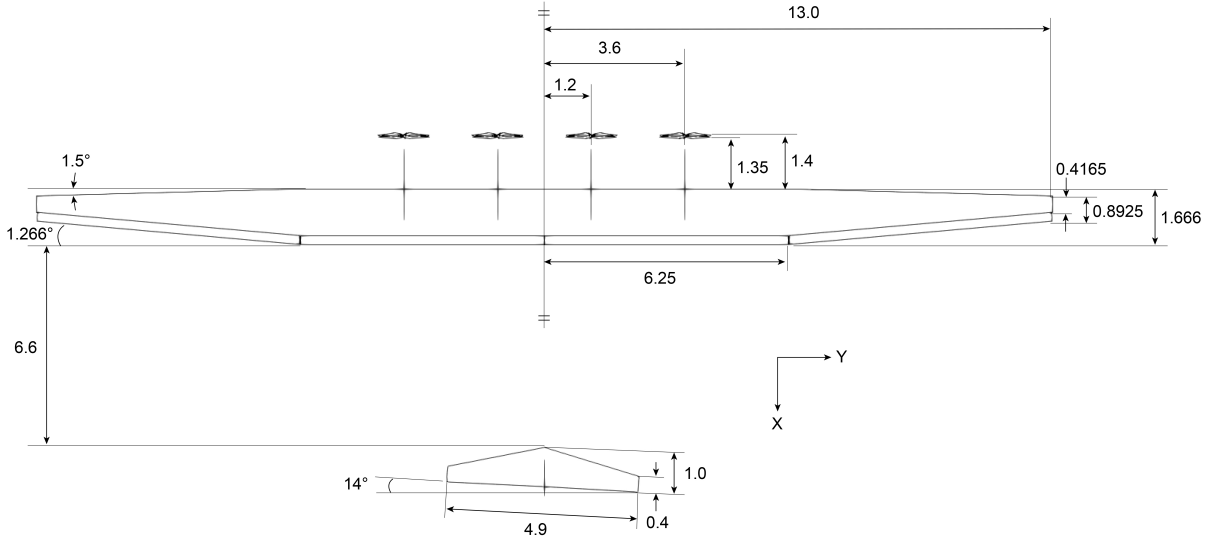
A. Windcraft Geometry

Fig. 14   Top view of our geometry approximation details.
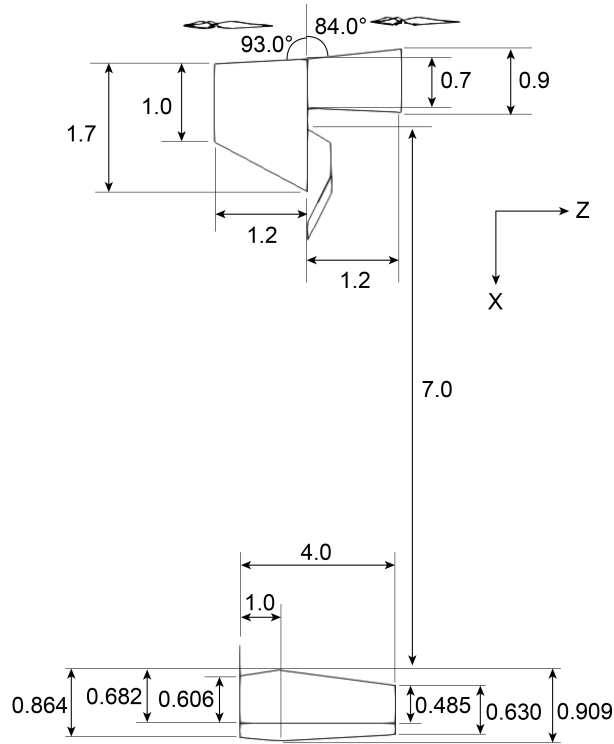
Fig. 15   Side view of our geometry approximation details.
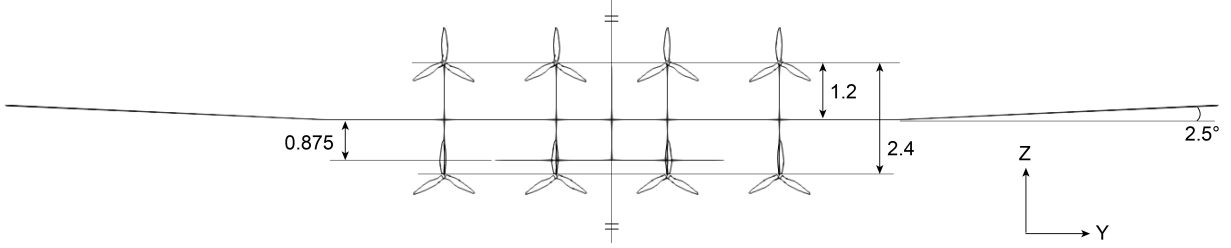
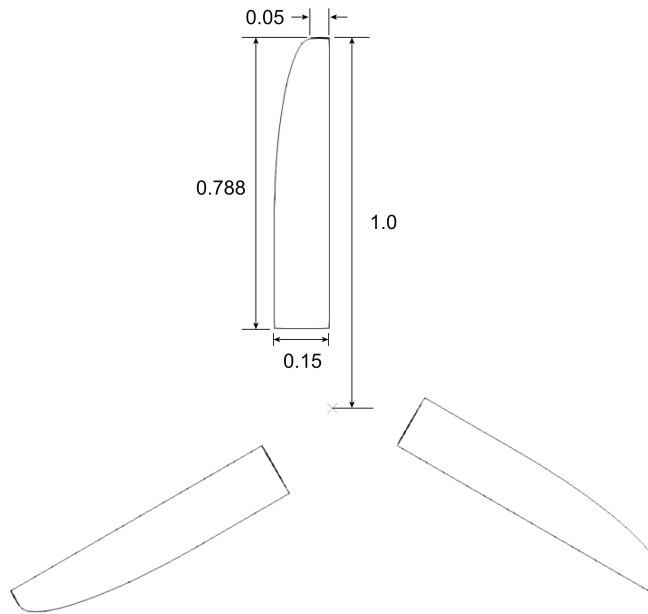**Fig. 16   Back view of our geometry approximation details.**

Fig. 17   Front view of our rotor design.   The chord and twist distributions are defined in equation (1) and equation (3), respectively.